ARL-TR-8496 ● SEP 2018

US Army Research Laboratory

# Aerodynamic Model for Canard Control Actuation on a Subsonic, Gun-Launched Munition

by Joshua T Bryson, Ilmars Celmins, and Frank E Fresconi

Approved for public release; distribution is unlimited.

## NOTICES

### Disclaimers

ARL-TR-8496 ● SEP 2018

US Army Research Laboratory

# Aerodynamic Model for Canard Control Actuation on a Subsonic, Gun-Launched Munition

**by Joshua T Bryson, Ilmars Celmins, and Frank E Fresconi**
*Weapons and Materials Research Directorate, ARL*

## REPORT DOCUMENTATION PAGE

*Form Approved*
*OMB No. 0704-0188*

| | | |
|---|---|---|
| **1. REPORT DATE** *(DD-MM-YYYY)*<br>September 2018 | **2. REPORT TYPE**<br>Technical Report | **3. DATES COVERED (From - To)**<br>January 2018–April 2018 |

**4. TITLE AND SUBTITLE**
Aerodynamic Model for Canard Control Actuation on a Subsonic, Gun-Launched Munition

**5a. CONTRACT NUMBER**

**5b. GRANT NUMBER**

**5c. PROGRAM ELEMENT NUMBER**

**6. AUTHOR(S)**
Joshua T Bryson, Ilmars Celmins, and Frank E Fresconi

**5d. PROJECT NUMBER**

**5e. TASK NUMBER**

**5f. WORK UNIT NUMBER**

**7. PERFORMING ORGANIZATION NAME(S) AND ADDRESS(ES)**
US Army Research Laboratory
ATTN: RDRL-WML-E
Aberdeen Proving Ground, MD 21005

**8. PERFORMING ORGANIZATION REPORT NUMBER**
ARL-TR-8496

**9. SPONSORING/MONITORING AGENCY NAME(S) AND ADDRESS(ES)**

**10. SPONSOR/MONITOR'S ACRONYM(S)**

**11. SPONSOR/MONITOR'S REPORT NUMBER(S)**

**12. DISTRIBUTION/AVAILABILITY STATEMENT**
Approved for public release; distribution is unlimited.

**13. SUPPLEMENTARY NOTES**

**14. ABSTRACT**

The US Army's modernization priority of long-range precision fires has identified a need for low-cost, high-g survivable, fast-responding munition control actuation technologies. This report investigates subsonic aerodynamics of canards mounted to a complex munition configuration. The results capture regions of attached, partially separated, and fully separated flow. A static aerodynamic model of the normal force and pitching moment was developed with a dependency on the canard deflection angle. Interactions of vortices shed off the canards onto the fins were offered to explain this behavior.

**15. SUBJECT TERMS**
canard control actuation system, canard aerodynamics, nonlinear aerodynamic model, wind tunnel, subsonic aerodynamics

| **16. SECURITY CLASSIFICATION OF:** | | | **17. LIMITATION OF ABSTRACT** | **18. NUMBER OF PAGES** | **19a. NAME OF RESPONSIBLE PERSON** |
|---|---|---|---|---|---|
| | | | | | Joshua T Bryson |
| **a. REPORT** | **b. ABSTRACT** | **c. THIS PAGE** | | | **19b. TELEPHONE NUMBER (Include area code)** |
| Unclassified | Unclassified | Unclassified | UU | 34 | 410-306-1939 |

Standard Form 298 (Rev. 8/98)
Prescribed by ANSI Std. Z39.18

## Contents

## List of Figures

## List of Tables

## Acknowledgments

The authors are grateful to Jubaraj Sahu for computational fluid dynamics visualizations and Clayton Moury and Daniel Everson from the Edgewood Chemical Biological Center at Aberdeen Proving Ground for conducting wind-tunnel experiments.

# 1. Introduction

The Army's modernization priority of long-range precision fires is motivating research into maneuvering munition technologies to provide range extension of gun-launched munitions through trajectory shaping as well as terminal maneuver authority to engage imprecisely located, moving, and protected targets with precision. Improving munition maneuverability is a multidisciplinary effort influenced by a variety of factors. This study is focused on understanding the aerodynamics and actuator and flight dynamics to develop canard control technologies.

A key challenge to developing actuation technologies for the gun-launched environment is the high-g loads imparted to electromechanical components during the gun-launch event.[1] Additionally, the flight velocities and flight dynamics characteristics typically result in actuator performance requirements that demand a fast, precise response while overcoming the aerodynamic loads.

Cost is a significant constraint as well. The control actuation system is typically a significant driver of guided munition cost, and more expensive munitions are purchased in smaller quantities and employed more sparingly. Prioritizing low-cost control actuation technologies helps preserve the high-volume fire capabilities typical of gun-based weapon systems, while improving the range and terminal control authority maneuverability of the munition and providing range.

Currently fielded gun-launched guided munitions make use of tactical missile or aerospace actuator technologies and harden them for the high-g gun launch.[2,3] These high-performance actuators provide desired maneuverability, but they are expensive. Recent research has successfully demonstrated an under-actuated solution that uses fewer actuators to reduce cost by dithering a canard in phase with the projectile spin.[4–7] However, this inherent modulation of the control surface means this approach is better suited to small course corrections and is not well suited to high-maneuverability applications. Other maneuverability research has pursued the generation of asymmetric aerodynamic forces on the projectile body by injecting pulsed jets[8] or plasma into the flow,[9] or by modulating protrusions to create desirable shock interactions on fixed fins.[10,11] These approaches are survivable to high-g loads, but offer limited maneuverability and are only effective across limited flight regimes. Another approach uses piezoelectric actuators to morph an airfoil.[12] This concept is also well suited to high-g launch survivability, but offers only limited maneuverability due to the power requirements of piezoelectric actuation over large deflections.

The overarching goal of this research is to realize low-cost, fast-responding, high-g tolerant control actuation technologies for guided munitions. Low-cost, commercial off-the-shelf technologies are adapted into a high-g survivable, independent canard control actuator that meets flight performance requirements. This report describes efforts to understand the subsonic, 3-D aerodynamics of the canard on the body to validate computational modeling results, reduce actuator hinge moment, improve flight modeling, understand airframe maneuver authority, and improve actuator dynamic modeling and control.

This report is organized as follows: the actuator and technology demonstration airframe are described in Section 2, the wind tunnel experiment and apparatus are presented in Section 3, and the aerodynamic model is formulated in Section 4. The wind tunnel experiment results are presented in Section 5 and analyzed in Sections 6–9. The models for canard aerodynamic normal force and hinge moment are presented in Section 10.

## 2. Airframe and Control Actuation

Figure 1 illustrates a high-maneuverability airframe (HMA) used for technology demonstration purposes. The munition is 83 mm in diameter, 420 mm long, weighs about 3.3 kg and flies in the subsonic regime after experiencing up to 10,000 g's of acceleration during gun launch. The vehicle features eight fixed fins in the rear for stabilization and four moveable canards toward the nose for control.[13]

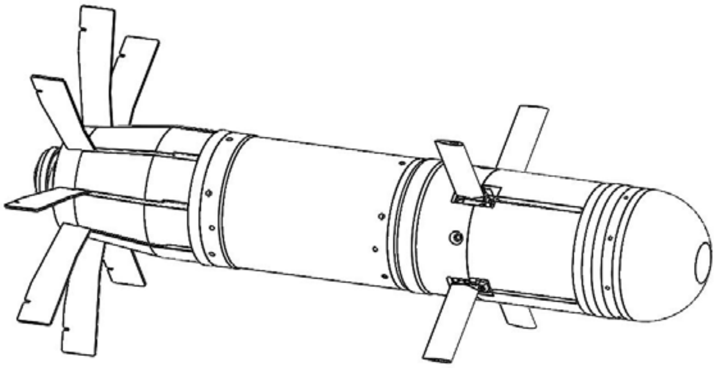

**Fig. 1 The 83-mm, gun-launched, HMA showing the four independently controlled canards near the projectile nose**

The control actuation system (CAS) consists of four independently controlled canards, each actuated using an E-flite EFLRDS76T servomotor (hereafter referred to as servo) through a rigid bar linkage.[14] Each canard has a ±10° range of deflection. Figure 2 shows the EFLRDS76T stock servomotor, and Fig. 3 shows the servomotor integrated into the CAS, actuating the canard through a linkage.

**Fig. 2 The E-flite EFLRDS76T off-the-shelf servo used in the CAS**

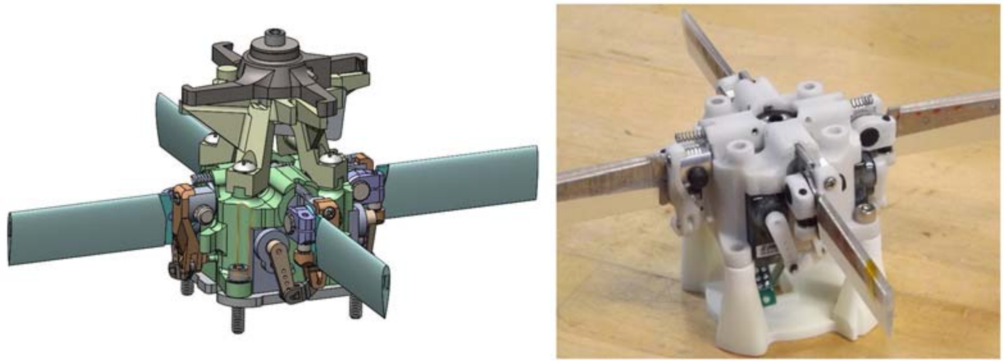

**Fig. 3 The CAS showing the servo actuating the canard blade**

The canard blade is rotated through a linkage attached to the servo output shaft. During flight, the aerodynamic forces on the canard blade generate hinge moments on the canard that must be counteracted by the servo to hold the desired canard deflection. To minimize the effort required to maintain the canard deflection against the aerodynamic loads, the canard rotation hinge was placed close to the estimated center of pressure (CP) calculated from the results of computational fluid dynamics (CFD) modeling. However, as the location of this aerodynamic CP with respect to the canard hinge axis is a significant factor determining the canard hinge moment, one goal of this series of experiments is to refine the CP location estimate and decrease the uncertainty.

The canard has a NACA-0015 profile, with a chord of 18.86 mm and a wetted length of 57.02 mm for an exposed planform area of 1075.39 mm$^2$. The canard hinge is 138.4 mm measured from the projectile nose and is located 2.81 mm aft of the canard leading edge, as shown in Fig. 4, putting the pivot line at 15% of the chord. This location is chosen to be 1 mm in front of the CP estimated from CFD calculations to minimize aerodynamic hinge loading over the expected ranges of angle of attack of the canard while maintaining a stabilizing, restoring moment on the canard.

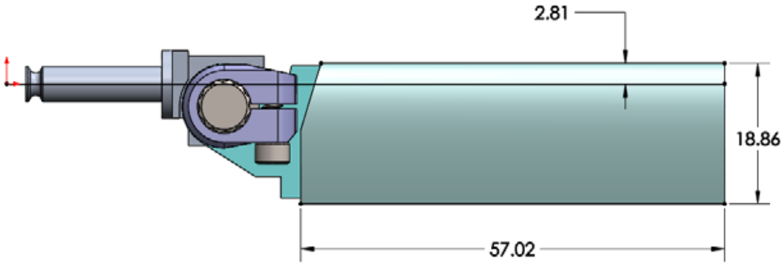

**Fig. 4 Canard assembly showing location of pivot line relative to canard blade; dimensions in millimeters**

## 3. Wind Tunnel Experiment Apparatus

The goal of the wind tunnel experiment is to measure the hinge moment experienced by the canard at different angles of attack and to improve the CP location estimates. The aerodynamic forces and moments on the canard are expected to vary as a function of both canard deflection angle and body angle of attack due to interactions in the flow around the body and the blade.

The experiment apparatus was designed to house a torque sensor (Mark-10 MTT03-20Z) attached to a vertical canard blade. The torque sensor was enclosed inside a beam extending below the projectile, and the canard blade axle was supported by a pair of bearings to minimize rotational friction and resist the lateral force loads, as illustrated in Fig. 5. To improve the accuracy of the experiment and capture the 3-D interaction effects between the body and blade, the physical model was designed with the same outer mold line as the HMA munition and includes canard deployment slots in the body as well as canards and fins, as shown in Fig. 6.

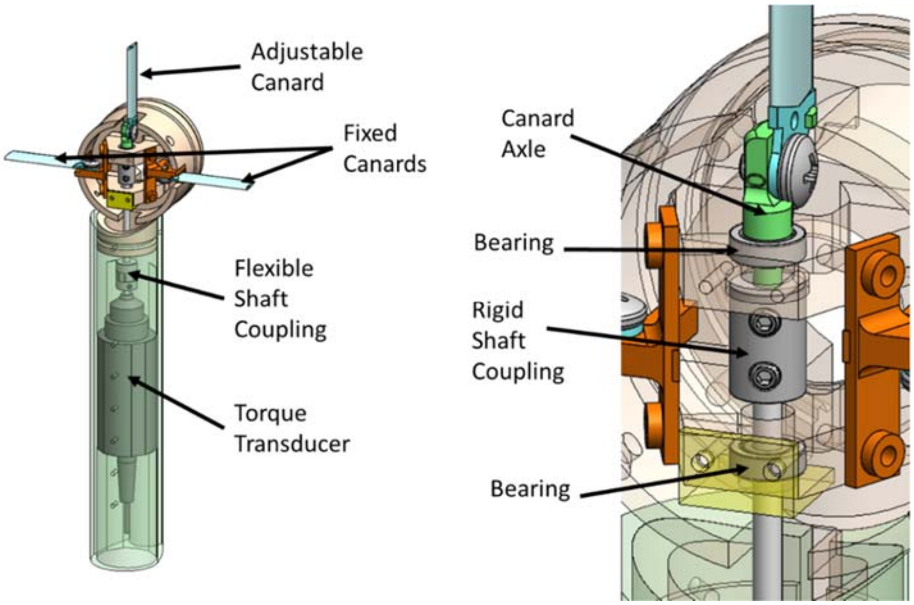

**Fig. 5 Canard mounting fixture and torque sensor location**

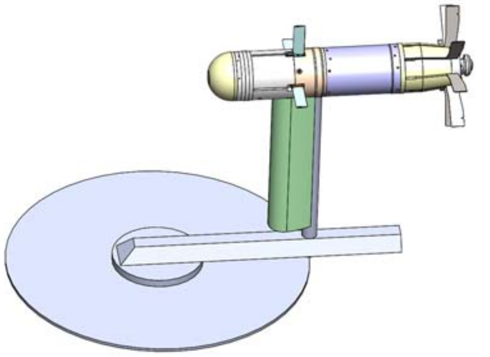

**Fig. 6 Wind tunnel apparatus. The vertical canard is replaceable to vary the canard deflection angle and the hinge location, while the fixture can be rotated to change the body angle of attack.**

The wind tunnel chosen for this experiment is large enough to accommodate the full-scale model, but is only capable of Mach 0.2, while the intended launch velocity is Mach 0.6. Although force and moment data in the form of aerodynamic coefficients can easily be scaled across subsonic Mach numbers, the magnitude of the aerodynamic forces in this experiment is expected to be approximately 11 times smaller than those at Mach 0.6. Additionally, as previously described, the canard hinge is designed to be close to the CP location, so the moment introduced by aerodynamic forces is small. These two factors combine to create concern about accurately measuring the hinge moment in this experiment above the sensor noise. To improve the ability to accurately measure the moment on the canard hinge in this experiment, a set of modified canards is used that have the same airfoil shape but have modified hinge locations, as shown in Fig. 7. Hinge locations farther from the CP will have a larger moment arm to amplify the effect of the aerodynamic forces, and by using canards with a range of hinge locations, the CP location can be more accurately estimated.

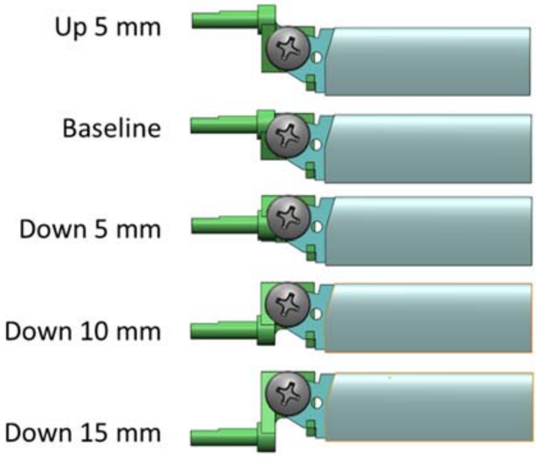

**Fig. 7 Set of modified canard blades with varying hinge locations**

The wind tunnel is equipped with a rotating table to adjust the body angle of attack with respect to the airflow. In order to accurately adjust the canard deflection angle in a repeatable way, multiple canards were created with flats on the axles designed to mate with a set screw at the desired deflection angle, as shown in Fig. 8. Additionally, a pointer tool that fits over the canard blade is used to verify the deflection angle with a set of index holes after each blade change, as shown in Fig. 9.

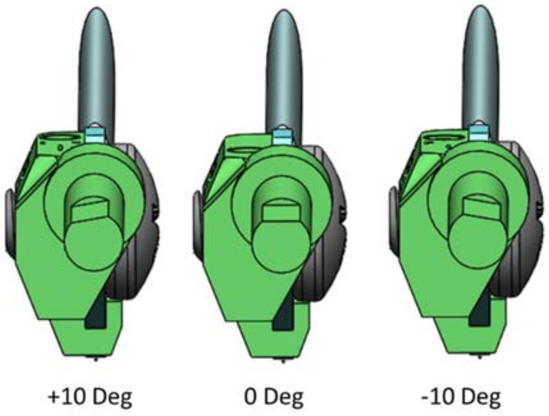

**Fig. 8 Canard axles showing the flats used to align the canard at a desired deflection angle using a set screw. Axles with flats at ±5° were also created, but are not shown.**

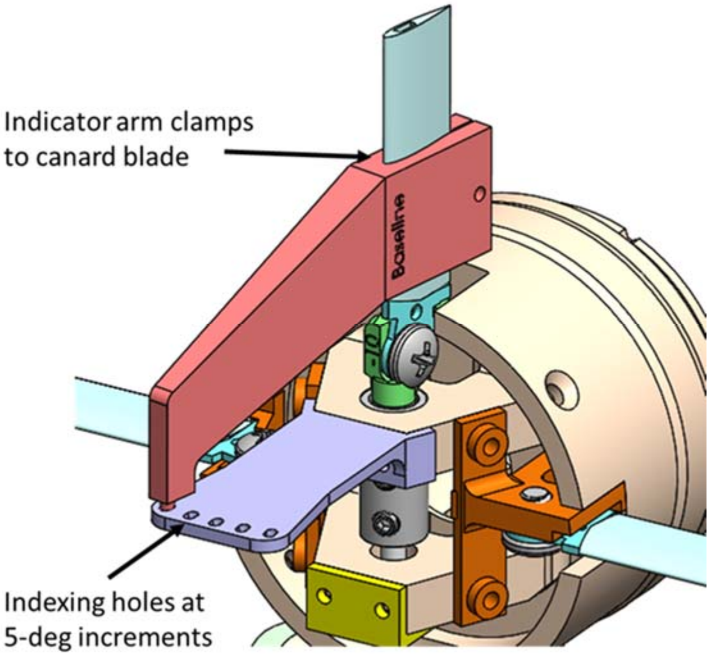

**Fig. 9** **Indicator arm used to verify the canard deflection angle set using the axle flats**

The wind tunnel experiment is designed to measure the moment about the canard hinge for varying canard deflection angles, canard hinge locations, and body attack angles. The range of each independent parameter for this experiment is described in Table 1. In the nominal design, the canard hinge is 138.4 mm measured from the nose, but the experiment refers to canard hinge location as an offset from the nominal location, with positive offset closer to the nose.

**Table 1** **Wind tunnel experiment parameters**

| Independent parameter | Range in experiment |
|---|---|
| Canard deflection angle, $\delta$ | –10°, –5°, 0°, 5°, 10° |
| Body angle of attack, $\alpha$ | -20°, –19°, … , 19°, 20° |
| Canard hinge location, $\Delta x$ | +5 mm, 0 mm, –5 mm, –10 mm, –15 mm |

The body and other custom parts in this apparatus were fabricated by the Rapid Technologies and Inspection Branch of the Advanced Design and Manufacturing Division of the Edgewood Chemical Biological Center, located at the Edgewood Area of Aberdeen Proving Ground, Maryland, using the selective laser sintering process on a 3D Systems Sinterstation 2500 plus with Advanced Laser Materials PA614-GS Nylon material. The canard airfoil is made from DSM SOMOS 11122

WaterShed-XC on the 3D Systems SLA-Viper, and has a 7075-T6 waterjet cut aluminum core to add stiffness.

## 4. Aerodynamic Model

The wind tunnel experiment measures canard hinge moment, $M_{hinge}$, which is generalized into coefficient form using the following equation:

$$M_{hinge} = QSD * C_m, \tag{1}$$

where $C_m$ is the canard hinge moment coefficient, $Q$ is the dynamic pressure, $S$ is the aerodynamic reference area, and $D$ is the reference diameter. The $QSD$ factor is calculated as shown:

$$QSD = \left(\frac{1}{2}\rho V^2\right) * \left(\frac{\pi}{4}D^2\right) * D. \tag{2}$$

For this experiment, the reference diameter, $D$, is 0.083 m, the free air velocity, $V$, is 58 m/s, and the atmospheric density, $\rho$, is 1.2923 kg/m$^3$.

The hinge moment on the canard is a result of the aerodynamic normal force, $F_N$, on the canard acting at a CP offset from the hinge. The separation distance between the CP and the hinge location is termed $d_{CP}$, and the separation vector creates a moment arm about the hinge and induces a hinge moment as shown:

$$M_{hinge} = F_N d_{CP}. \tag{3}$$

The location of the canard CP can be calculated by interpolating the $C_m$ from different hinge locations to find the hinge location of zero moment. This zero moment point occurs when the aerodynamic CP is aligned with the canard hinge location ($d_{CP} = 0$) such that no moment is produced from the aerodynamic force.

Using the calculated canard CP location and the measured hinge moment, the normal force coefficient, $C_N$, on the canard is calculated as follows:

$$C_N = \frac{D}{d_{CP}} C_m. \tag{4}$$

The total canard angle of attack, $\alpha_c$, is defined as the sum of the canard deflection angle, $\delta$, and the component of the body attack angle in the plane perpendicular to the canard rotation axis, $\alpha_\perp$, as shown:

$$\alpha_c = (\alpha_\perp + \delta). \tag{5}$$

This research develops an aerodynamic model for the canard, relating $C_N$ and $C_m$ on the canard to both $\delta$ and $\alpha_c$. However, as $\alpha_c$ only considers the perpendicular component of the body attack angle, this model does not consider the effect of the remaining body attack angle components parallel to the canard rotation axis. Both

$\delta$ and $\alpha_\perp$ contribute to $C_N$ and $C_m$ and allow modeling of some of the secondary interaction effects. A more complete aerodynamic model would account for the effects of all body attack angle components, but the additional wind tunnel experiments required to characterize those effects were deemed outside the scope of effort for this research.

The canard $C_N$ model is formulated as a fifth-order polynomial in the form

$$C_N(\delta) = C_{N0}(\delta) + C_{N\alpha_c}(\delta)\sin(\alpha_c) + C_{N\alpha_c^3}(\delta)\sin^3(\alpha_c) + C_{N\alpha_c^5}(\delta)\sin^5(\alpha_c) \quad (6)$$

for canard deflection angle, $\delta$, and total canard angle of attack, $\alpha_c$, both in radians. The canard $C_m$ model is formulated as a third-order polynomial, with the hinge moment referenced from the nominal hinge location, with each polynomial in the form

$$C_m(\delta) = C_{m0}(\delta) + C_{m\alpha_c}(\delta)\sin(\alpha_c) + C_{m\alpha_c^3}(\delta)\sin^3(\alpha_c) \quad (7)$$

for canard deflection angle, $\delta$, and total canard angle of attack, $\alpha_c$, both in radians. The regions of attached flow, partial separation, and separated flow are each expressed as separate polynomials in the model, and the goal of the wind tunnel experiment is to establish the boundaries of the flow regimes, along with the $C_{N0}$, $C_{N\alpha_c}$, $C_{N\alpha_c^3}$, $C_{N\alpha_c^5}$ and the $C_{m0}$, $C_{m\alpha_c}$, $C_{m\alpha_c^3}$ coefficients describing the polynomial data fit in each region.

## 5. Experiment Results

As described in Table 1, the hinge load on the canard was measured in the wind tunnel at each body angle of attack ranging from –20° to 20° in 1° increments for each canard deflection angle and hinge location. The canard deflection angle, $\delta$, was varied from –10° to 10° in 5° increments, while the canard hinge location was varied from +5 mm to –15 mm in 5-mm increments from the nominal location. The hinge moments measured for each canard configuration along the sweep of body attack angle are plotted in Fig. 10.

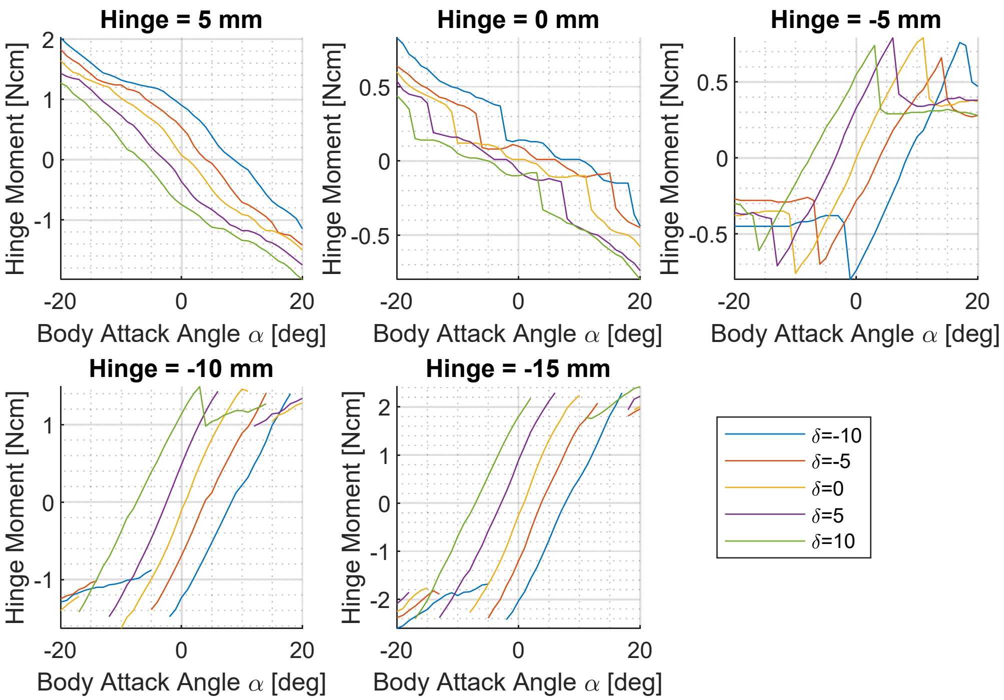

**Fig. 10 Canard hinge moment measurements as a function of body angle of attack, $\alpha$, for different fixed canard deflection angles, $\delta$**

By adding the canard deflection angle to the perpendicular component of the body angle of attack, the total attack angle, $\alpha_c$, of the canard is calculated, as shown in Eq. 5. Figure 11 plots the measured hinge moments for each canard configuration across total angle of attack.

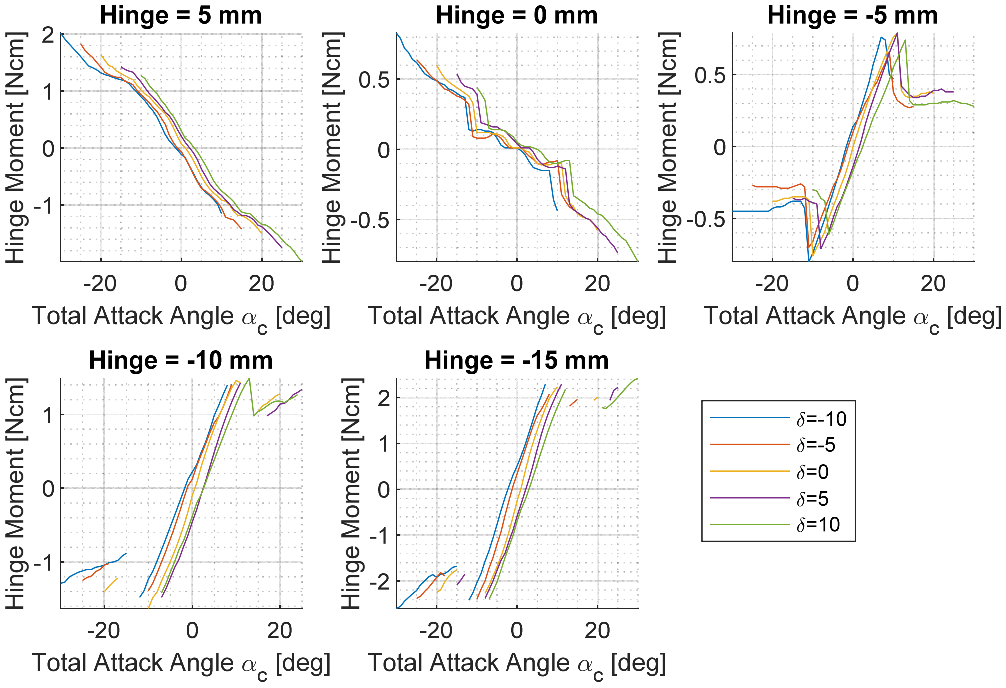

**Fig. 11 Canard hinge moment measurements as a function of total angle of attack, $\alpha_c$, for fixed canard deflection angles, $\delta$**

Inspection of Figs. 10 and 11 reveals interaction effects between the body and canard, as indicated by the consistent, systematic offset of the hinge moment data according to deflection angle. The –10° deflection cases have a consistently positive offset at equivalent total attack angles, while the +10° deflection cases have consistent negative offset. The +5° and –5° deflection cases exhibit similar offsets.

In both sets of figures, the slope of the data for the nominal hinge location (0 mm) and the +5 mm hinge location are negative, indicating the CP is behind the hinge due to the restoring moment toward zero deflection generated by the aerodynamic normal force on the canard. As the hinge location is moved back (–5 mm to –15 mm), the slope of the data changes to positive, indicating the CP is forward from the hinge due to the destabilizing moment. The magnitude of the measured hinge moment increases as the hinge location is moved from the nominal 0 mm position, indicating the canard CP is located close to the nominal hinge axis.

## 6. Canard Hinge Moment Coefficient

Using Eq. 1, the canard hinge moment is converted to moment coefficient, $C_m$. Figure 12 plots $C_m$ as a function of total angle of attack for all canard configurations.

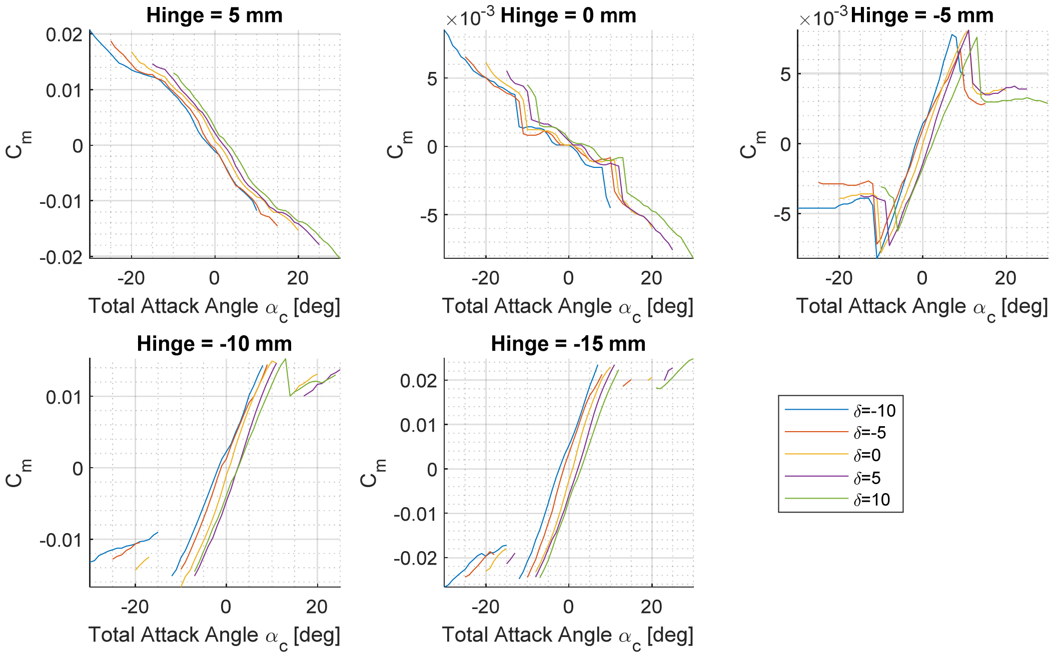

**Fig. 12 Canard hinge moment coefficient, $C_m$, as a function of total angle of attack, $\alpha_c$, for fixed canard deflection angles, $\delta$**

## 7. Canard Center of Pressure

Using Eq. 4, the $C_m$ data from each hinge location are analyzed to extract the canard CP location. Figure 13 plots $C_m$ versus hinge location across $\alpha_c$, with each canard deflection angle graphed separately. In each case, the lines for lower angles of attack (–5° to +5°) cross the horizontal axis just negative of the nominal hinge location, indicating the CP location for attached flow. Flow separations at the more-extreme angles of attack are seen to move the CP to a more negative location with respect to the nominal hinge.

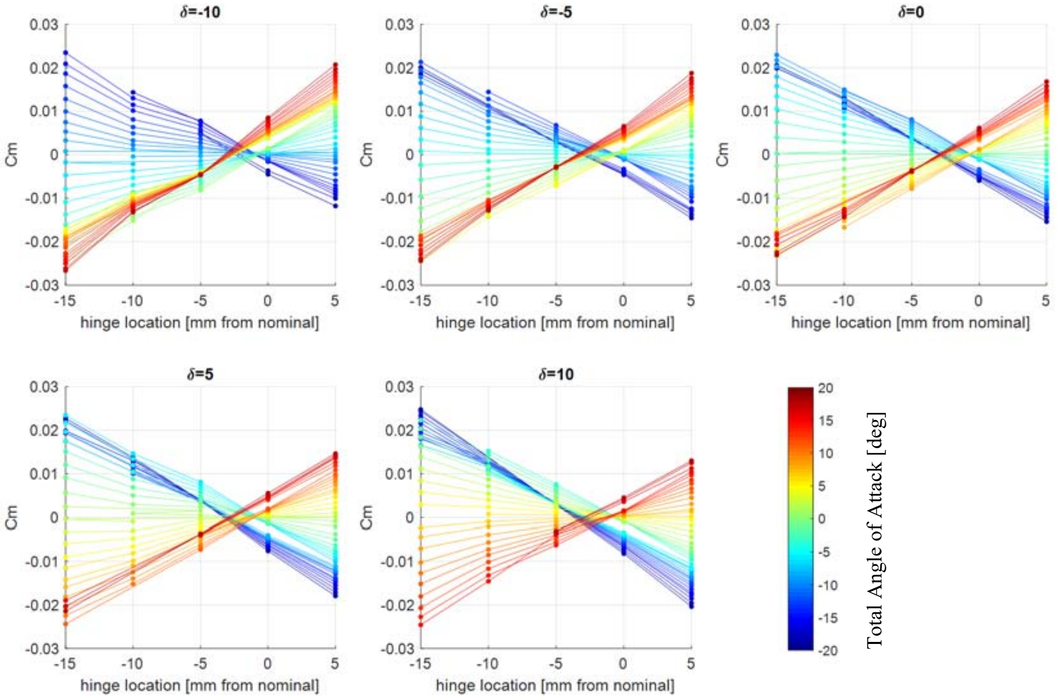

**Fig. 13 Cm vs. canard hinge location across angle of attack. The data for each canard deflection angle are plotted separately.**

The CP locations from all canard deflection angles are plotted together in Fig 14, along with the nominal hinge location and the one-quarter chord location. The figure also includes previous Navier-Stokes CFD modeling results for the canard CP, which were used to inform the nominal canard hinge placement.[15,16] The wind tunnel experiment compares favorably with the CFD modeling for attached flow conditions.

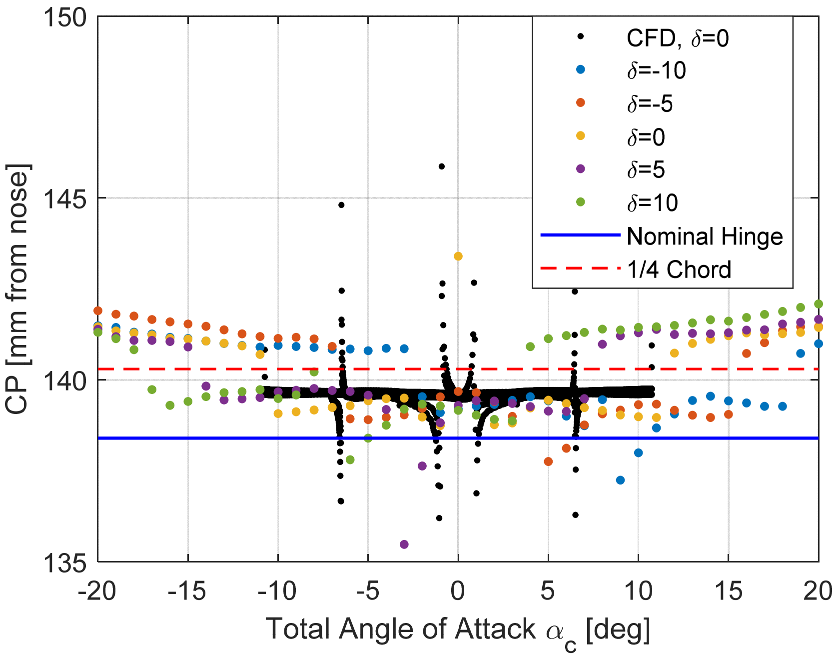

**Fig. 14 Wind tunnel measurements of CP location vs. total angle of attack data for all canard deflection angles plotted alongside CFD data. The nominal canard hinge location and the one-quarter chord location are shown for reference.**

## 8. Aerodynamic Analysis for 0° Canard Deflection

The wind tunnel measurements for $\delta = 0°$ are first analyzed as a stand-alone set of data, before being combined together with all deflection angles in the larger set of data. Using Eq. 4, the $C_N$ is calculated from the $C_m$ and the CP location. Figure 15 plots $C_N$ versus $\alpha_c$ for $\delta = 0°$ at each hinge location, along with the $C_N$ obtained through CFD. CFD results compare well to wind tunnel data, especially prior to flow separation. The plot illustrates the relationship between the normal force and the flow behavior for attached, partially separated, and fully separated flow regimes. Under attached flow conditions at small angles of attack, the increasing pressure differential between upper and lower canard surfaces increases the force as the attack angle increases. Larger angles of attack create adverse pressure gradients that give rise to complex 3-D, transient flow structures (stall cells). Stall cells are formed around physical imperfections on the low-pressure side of the airfoil that yield small, localized separation bubbles. Vorticity ensues in the spanwise direction as the flow swirls behind the separation bubble. This process is depicted in the CFD visualizations of Fig. 16 and described further in references such as Gad-el-Hak and Bushell.[17] These adverse pressure gradients encountered during partial separation reduce the pressure differential, and thereby reduce the force generated. The flow eventually transitions from partial separation to full separation as the angle of attack continues to increase.

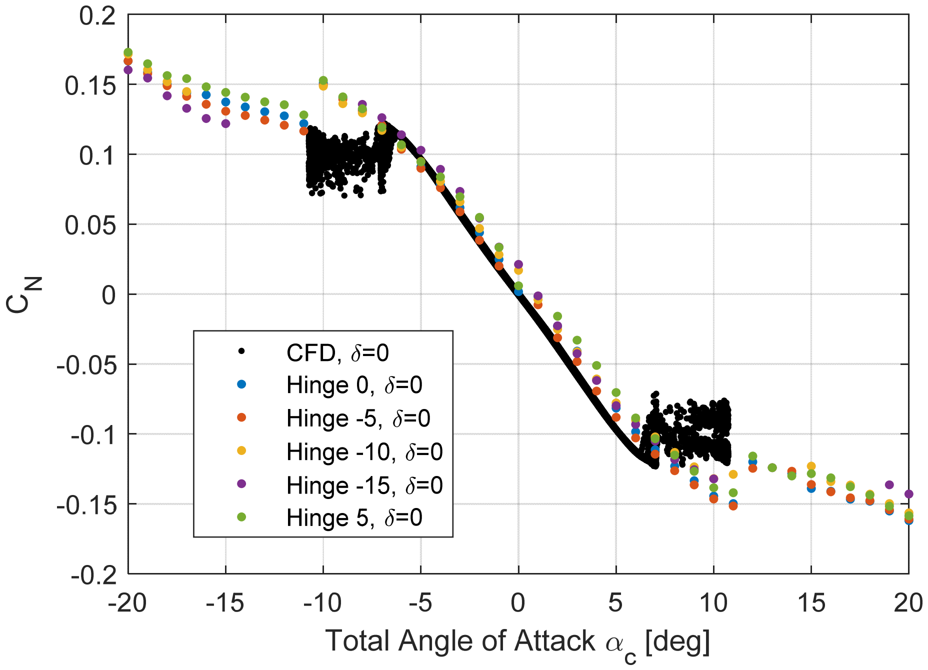

**Fig. 15** $C_N$ **vs. total angle of attack for 0° canard deflection angle at all hinge locations**

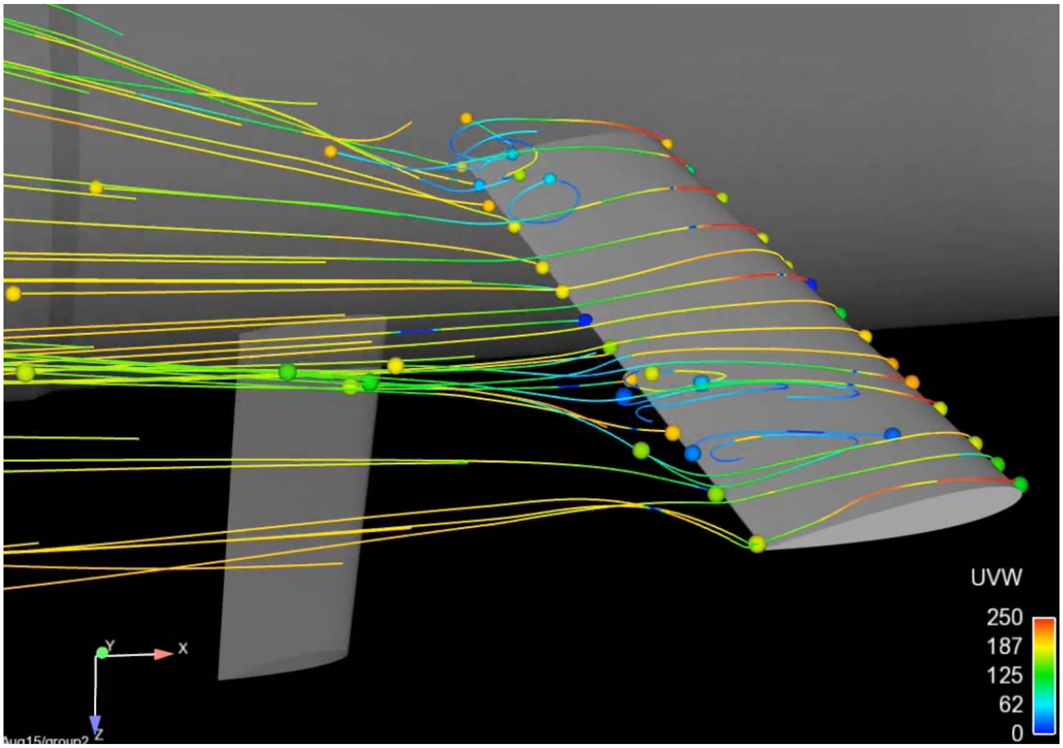

**Fig. 16** **Depiction of partial flow separation (stall cell) over low-pressure side of airfoil from CFD visualization**

Using the CP location and the nominal hinge location of 0.1384 m from the projectile nose, $C_N$ can be converted to $C_m$, referenced from the same moment arm. Figure 17 plots $C_m$ versus $\alpha_c$ for $\delta = 0°$ at each hinge location, converted to the nominal hinge moment reference center, with the CFD modeling results shown in black. The wind tunnel data are largely consistent with the CFD results for the attached flow and onset of flow separation. The level of agreement between computation and experiment is encouraging given the complexities of the 3-D canard effects and flow interactions. These results lend credibility for reliance on computation of subsonic aerodynamics over complex bodies in future research.

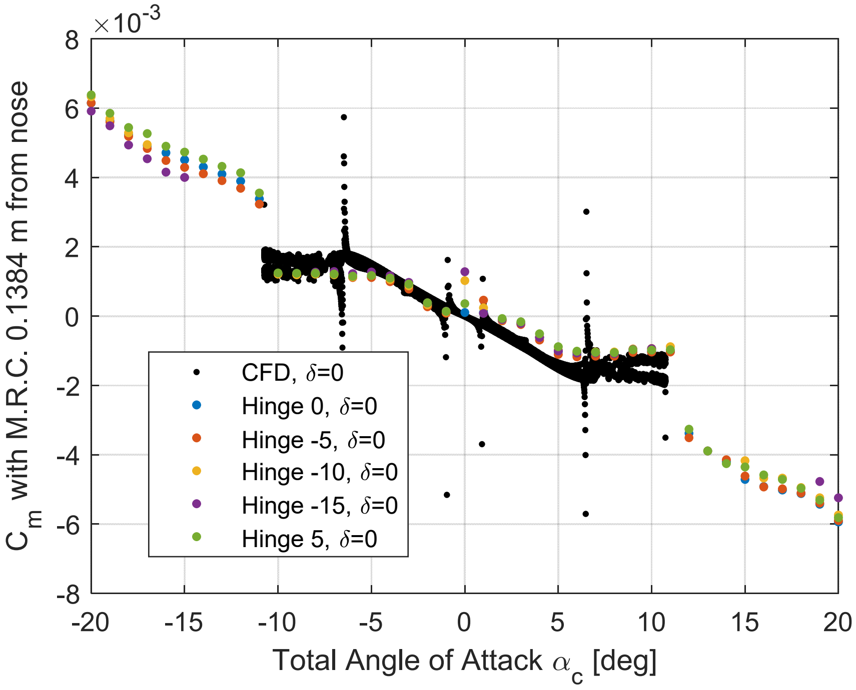

**Fig. 17 $C_m$ vs. total angle of attack for 0° canard deflection at all hinge locations. The moments are all referenced from the nominal hinge location to facilitate comparison of the data.**

## 9. Aerodynamic Analysis across Canard Deflection

The $\delta = 0°$ analysis process is repeated for the data at all other canard deflection angles. Figure 18 plots $C_N$ versus $\alpha_c$ for all hinge locations at each deflection angle, along with the CFD generated $C_N$. The data for each deflection angle are regressed with a piecewise fifth-order polynomial, as described in Eq. 6. The data exhibit a systematic offset that appears to be a function of deflection angle, which is likely due to interaction effects between the projectile body and the canard blade modulating the aerodynamic forces experienced by the blade at different local angles of attack.

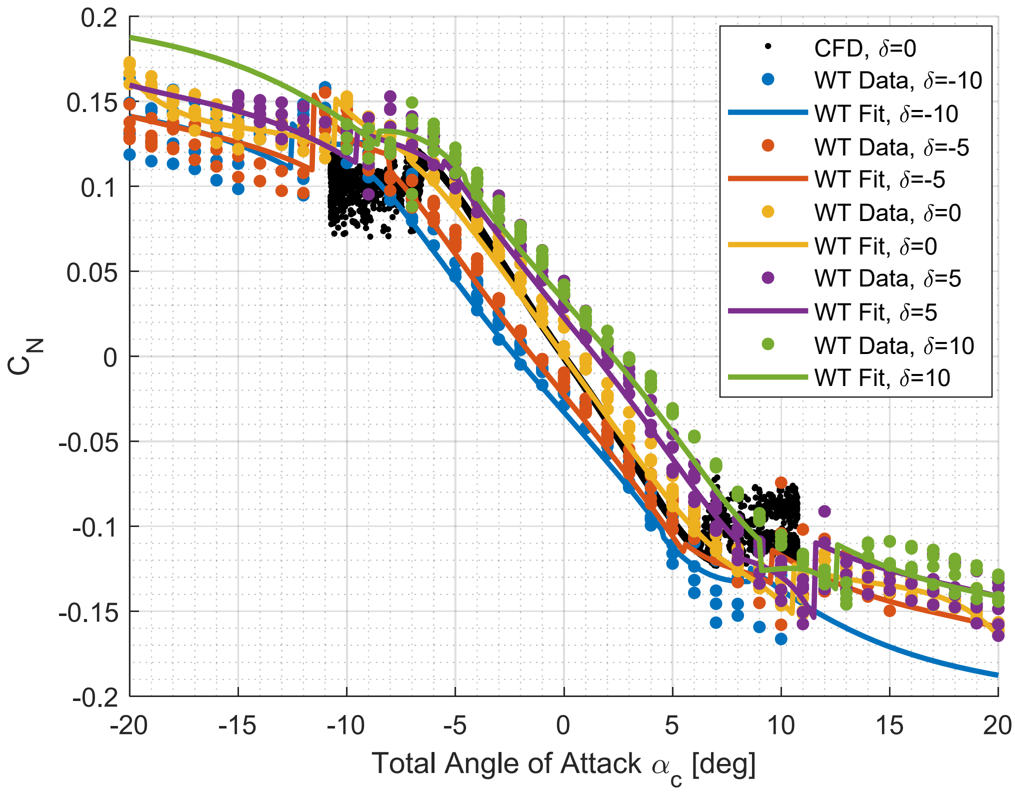

**Fig. 18 $C_N$ vs. total angle of attack for all hinge locations at each canard deflection angle. Fifth-order piecewise polynomial fit lines are plotted for each deflection angle dataset.**

Using the CP location and the nominal hinge location of 0.1384 m from the projectile nose, the $C_N$ values are converted to $C_m$, referenced with the same moment arm. Figure 19 plots $C_m$ versus $\alpha_c$ for all hinge locations at each deflection angle, converted to the nominal hinge moment reference center. CFD modeling results are again shown in black. The data for each deflection angle are fitted with a piecewise third-order polynomial following Eq. 7.

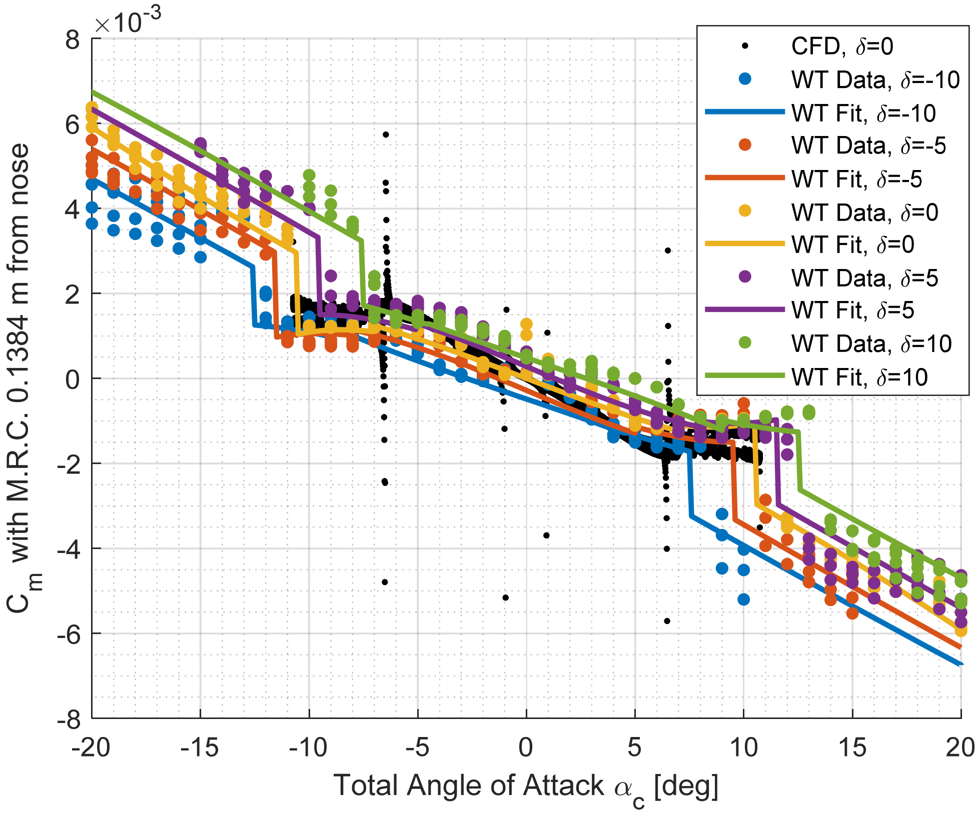

**Fig. 19 $C_m$ vs. total angle of attack for all canard deflection at all hinge locations. The moments are referenced from the nominal hinge location. Third-order piecewise polynomial fit lines are shown for each deflection angle dataset.**

## 10. Canard Aerodynamic Model

An aerodynamic model is created from the wind tunnel data, which describes $C_N$ and $C_m$ as a function of canard deflection and total angle of attack. This model can be used to improve the dynamic modeling and controllers and to increase the accuracy of simulation results.

The canard aerodynamic model is developed using an aerodynamic reference diameter of 0.083 m, with a moment reference center of 0.1384 m, measured from the projectile nose. The underlying data were collected at Mach 0.175, at a Reynold's number of $3.137 \times 10^5$.

The canard $C_N$ model is constructed from the set of piecewise fifth-order polynomials shown in Fig. 17, each having the form presented in Eq. 6, and repeated here for convenience:

$$C_N(\delta) = C_{N0}(\delta) + C_{N\alpha_c}(\delta)\sin(\alpha_c) + C_{N\alpha_c^3}(\delta)\sin^3(\alpha_c) + C_{N\alpha_c^5}(\delta)\sin^5(\alpha_c). \quad (8)$$

The boundaries of the aerodynamic flow regions identified from the experiment data are listed in Table 2. Each flow regime has a separate polynomial fit, with the $C_{N0}$, $C_{N\alpha_c}$, $C_{N\alpha_c^3}$, $C_{N\alpha_c^5}$ coefficients for each region given in Tables 3–5.

**Table 2 Flow regime boundaries for the canard aerodynamic model**

| $\boldsymbol{\delta}$ | Attached flow | Partial separation | Separated flow |
|---|---|---|---|
| 10° | $-9^{\circ} < \alpha_c < 4.5^{\circ}$ | $-12.5^{\circ} \leq \alpha_c \leq -9^{\circ}$<br>$4.5^{\circ} \leq \alpha_c \leq 8.5^{\circ}$ | $\alpha_c < -12.5^{\circ}$<br>$\alpha_c > 8.5^{\circ}$ |
| 5° | $-8^{\circ} < \alpha_c < 5.5^{\circ}$ | $-11.5^{\circ} \leq \alpha_c \leq -8^{\circ}$<br>$5.5^{\circ} \leq \alpha_c \leq 9.5^{\circ}$ | $\alpha_c < -11.5^{\circ}$<br>$\alpha_c > 9.5^{\circ}$ |
| 0° | $-7^{\circ} < \alpha_c < 7^{\circ}$ | $-10.5^{\circ} \leq \mathrm{\alpha}_\mathrm{c} \leq -7^{\circ}$<br>$7^{\circ} \leq \alpha_c \leq 10.5^{o}$ | $\alpha_c < -10.5^{\circ}$<br>$\alpha_c > 10.5^{\circ}$ |
| -5° | $-5.5^{\circ} < \alpha_c < 8^{\circ}$ | $-9.5^{\circ} \leq \alpha_c \leq -5.5^{\circ}$<br>$8^{\circ} \leq \alpha_c \leq 11.5^{\circ}$ | $\alpha_c < -9.5^{\circ}$<br>$\alpha_c > 11.5^{\circ}$ |
| -10° | $-4.5^{\circ} < \alpha_c < 9^{\circ}$ | $-8.5^{\circ} \leq \alpha_c \leq -4.5^{\circ}$<br>$9^{\circ} \leq \alpha_c \leq 12.5^{\circ}$ | $\alpha_c < -8.5^{\circ}$<br>$\alpha_c > 12.5^{\circ}$ |

**Table 3 Canard $\boldsymbol{C_N(\delta)}$ vs. $\boldsymbol{\alpha_c}$ model coefficients for the attached flow region**

| $\boldsymbol{\delta}$ | Attached flow region | | | |
|---|---|---|---|---|
| | $\boldsymbol{C_{N0}(\delta)}$ | $\boldsymbol{C_{N\alpha_c}(\delta)}$ | $\boldsymbol{C_{N\alpha_c^3}(\delta)}$ | $\boldsymbol{C_{N\alpha_c^5}(\delta)}$ |
| 10° | –0.032904 | –0.828982 | –10.223983 | 302.959326 |
| 5° | –0.022876 | –0.89664 | –10.522145 | 423.453021 |
| 0° | 0 | –1.021742 | 0.76091 | 358.119715 |
| –5° | 0.022876 | –0.89664 | –10.522145 | 423.453021 |
| –10° | 0.032904 | –0.828982 | –10.223983 | 302.959326 |

**Table 4 Canard $\boldsymbol{C_N(\delta)}$ vs. $\boldsymbol{\alpha_c}$ model coefficients for the partially separated flow regions**

| $\boldsymbol{\delta}$ | Partially separated region | | | |
|---|---|---|---|---|
| | $\boldsymbol{C_{N0}(\delta)}$ | $\boldsymbol{C_{N\alpha_c}(\delta)}$ | $\boldsymbol{C_{N\alpha_c^3}(\delta)}$ | $\boldsymbol{C_{N\alpha_c^5}(\delta)}$ |
| 10° | –0.003013 | –1.528516 | 39.374324 | –435.330436 |
| 5° | –0.003737 | –1.411679 | 38.834644 | –577.169402 |
| 0° | 0 | –1.260042 | 26.159355 | –393.547665 |
| –5° | 0.003737 | –1.411679 | 38.834644 | –577.169402 |
| –10° | 0.003013 | –1.528516 | 39.374324 | –435.330436 |

**Table 5 Canard $C_N(\delta)$ vs. $\alpha_c$ model coefficients for the separated flow regions**

| $\delta$ | Separated flow region | | | |
|---|---|---|---|---|
| | $C_{N0}(\delta)$ | $C_{N\alpha_c}(\delta)$ | $C_{N\alpha_c^3}(\delta)$ | $C_{N\alpha_c^5}(\delta)$ |
| 10° | –0.023233 | –0.741776 | 3.067993 | –6.942651 |
| 5° | –0.009123 | –0.727226 | 3.926957 | –12.281166 |
| 0° | 0 | –0.905312 | 8.431563 | –39.947116 |
| –5° | 0.009123 | –0.727226 | 3.926957 | –12.281166 |
| –10° | 0.023233 | –0.741776 | 3.067993 | –6.942651 |

Figure 20 plots the contour of the modeled $C_N$ surface as a function of body attack angle and canard deflection.

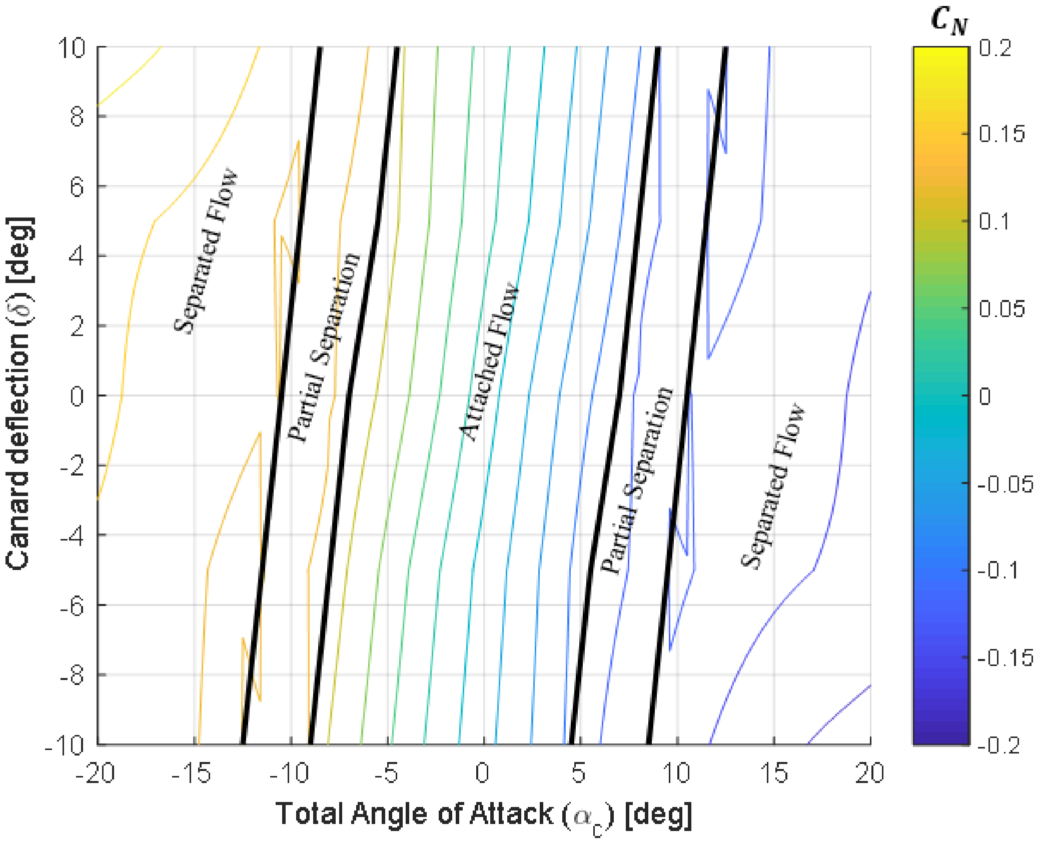

**Fig. 20 Plot of $C_N$ vs. total angle of attack, $\alpha_c$ and canard deflection angle, $\delta$ showing the regions of attached, partially separated, and fully separated flow**

The canard $C_m$ model is referenced from the nominal hinge location, and comprises a set of piecewise third-order polynomials shown in Fig. 19, each having the form presented in Eq. 7, and repeated here for convenience:

$$C_m(\delta) = C_{m0}(\delta) + C_{m\alpha_c}(\delta)\sin(\alpha_c) + C_{m\alpha_c^3}(\delta)\sin^3(\alpha_c) \quad (9)$$

for canard deflection angle $\delta$, and total canard angle of attack, $\alpha_c$ both in radians. The boundaries of the aerodynamic flow regions are kept consistent to the $C_N$ model, as listed in Table 2. Tables 6–8 present the $C_{m0}, C_{m\alpha}, C_{m\alpha 3}$ polynomial coefficients for each deflection angle, in each body attack angle domain.

**Table 6 Canard $C_m(\delta)$ vs. $\alpha_c$ model coefficients for the attached flow region**

| $\delta$ | Attached flow region | | |
|---|---|---|---|
| | $C_{m0}(\delta)$ | $C_{m\alpha_c}(\delta)$ | $C_{m\alpha_c^3}(\delta)$ |
| 10° | –0.000484 | –0.010002 | –0.034778 |
| 5° | –0.000281 | –0.012417 | 0.114927 |
| 0° | 0 | –0.011192 | 0.070548 |
| –5° | 0.000281 | –0.012417 | 0.114927 |
| –10° | 0.000484 | –0.010002 | –0.034778 |

**Table 7 Canard $C_m(\delta)$ vs. $\alpha_c$ model coefficients for the partially separated flow regions**

| $\delta$ | Partial separation region | | |
|---|---|---|---|
| | $C_{m0}(\delta)$ | $C_{m\alpha_c}(\delta)$ | $C_{m\alpha_c^3}(\delta)$ |
| 10° | –0.00067 | –0.009701 | 0.001939 |
| 5° | –0.000222 | –0.011512 | 0.138047 |
| 0° | 0 | –0.011603 | 0.176026 |
| –5° | 0.000222 | –0.011512 | 0.138047 |
| –10° | 0.00067 | –0.009701 | 0.001939 |

**Table 8 Canard $C_m(\delta)$ vs. $\alpha_c$ model coefficients for the separated flow regions**

| $\delta$ | Separated flow region | | |
|---|---|---|---|
| | $C_{m0}(\delta)$ | $C_{m\alpha_c}(\delta)$ | $C_{m\alpha_c^3}(\delta)$ |
| 10° | –0.001259 | –0.017687 | 0.004972 |
| 5° | –0.000468 | –0.017102 | 0.002432 |
| 0° | 0 | –0.015662 | –0.010454 |
| –5° | 0.000468 | –0.017102 | 0.002432 |
| –10° | 0.001259 | –0.017687 | 0.004972 |

Figure 21 plots the contour of the modeled $C_m$ surface as a function of body attack angle and canard deflection.

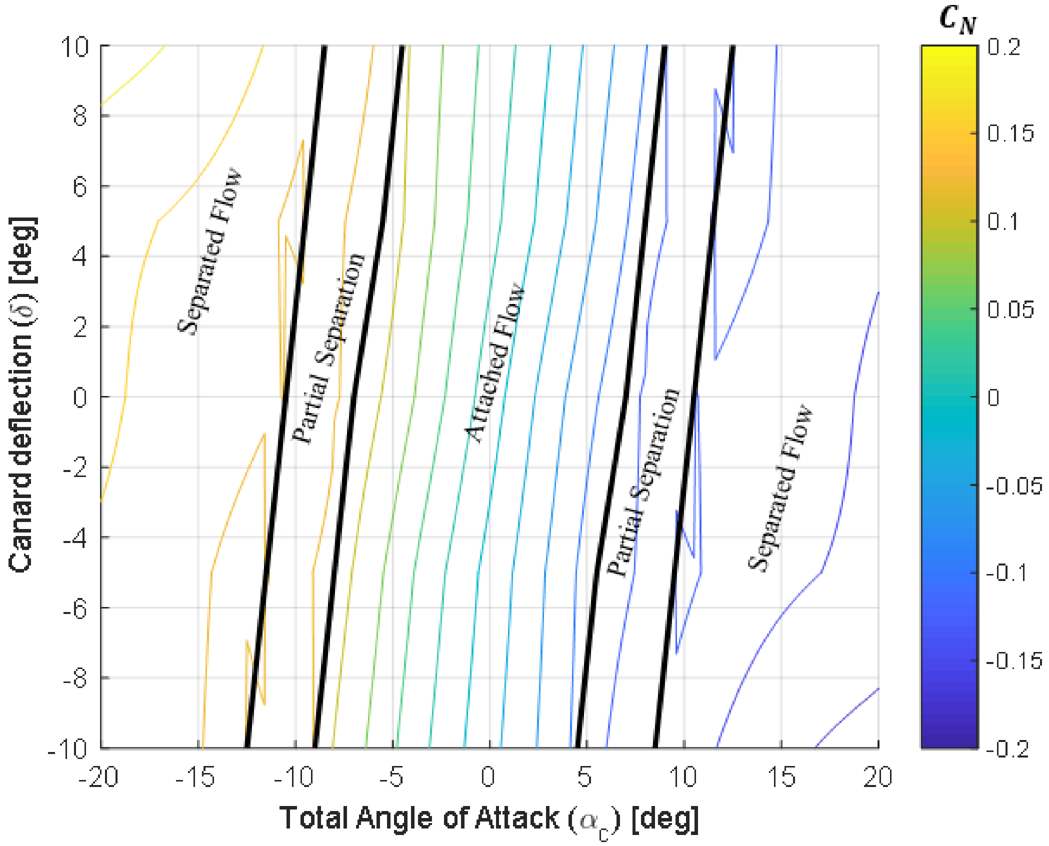

**Fig. 21 Plot of $C_m$ vs. total angle of attack and canard deflection angle, $\alpha_c$ and canard deflection angle, $\delta$ showing the regions of attached, partially separated, and fully separated flow**

## 11. Conclusion

This research characterized the subsonic aerodynamic forces and moments experienced by the 3-D canard on a body and developed a model for the normal force and pitching moments, which capture the nonlinear interactions between the canard deflection and body angle of attack. This model can be used to estimate the aerodynamic load on the actuator across the projectile flight envelope to develop a better understanding of actuator behavior during flight and can inform actuator design decisions to lower cost while maintaining required performance.

## 12. References

1. Carlucci DE, Frydman AM, Cordes JA. Mathematical description of projectile shot exit dynamics (set forward). Journal of Applied Mechanics 2013;80:031501-1–9.
2. Bender JM. Structural analysis of the Excalibur canard actuation system and the guidance and navigation unit. Aberdeen Proving Ground (MD): Army Research Laboratory (US). Report No.: ARL-TR-4412.
3. General Dynamics Ordnance and Tactical Systems. Missile Components. Control Actuator Systems (CAS). St Petersburg (FL): General Dynamics; c1995–2018 [accessed 2018 Aug 24]. https://www.gd-ots.com/missiles-and-rockets/missile-components/control_actuator_systems/.
4. Fresconi FE, Harkins T. Experimental flight characterization of asymmetric and maneuvering projectiles from elevated gun firings. Journal of Spacecraft and Rockets. 2012;49(6):1120–1130.
5. Fresconi FE. Guidance and control of a projectile with reduced sensor and actuator requirements. Journal of Guidance, Control, and Dynamics. 2011;34(6):1757–1766.
6. Fresconi FE, Brown G, Celmins I, DeSpirito J, Ilg M, Maley J, Magnotti P, Scanlan A, Stout C, Vazquez E. Very affordable precision projectile technology development and flight demonstrations. Aberdeen Proving Ground (MD): Army Research Laboratory (US); 2011. Report No.: ARL-TR-5460.
7. Fairfax L, Fresconi F, Maley J, inventors; US Secretary of Army, assignee. Method and apparatus for GPS-denied navigation of spin-stabilized projectiles. United States patent US 9,702,674. 2017 July 11.
8. McMichael J, Lovas A, Plostins P, Sahu J, Brown G, Glezer A. Microadaptive flow control applied to a spinning projectile. Aberdeen Proving Ground (MD): Army Research Laboratory (US); 2005. Report No.: ARL-TR-3589.
9. Gnemmi P, Rey C. Plasma actuation for the control of a supersonic projectile. Journal of Spacecraft and Rockets. 2009;46(5):989–998.
10. Kim D, Strickland L, Gross M, Rogers J, Costello M, Fresconi F, Celmins I. Actuator design and flight testing of an active microspoiler-equipped projectile. ASME. J Dyn Sys, Meas, Control. 2017;139(11):111002-111002-15. doi:10.1115/1.4036808.

11. Celmins I. Design and evaluation of an electromechanical actuator for projectile guidance. Aberdeen Proving Ground (MD): Army Research Laboratory (US); 2007. Report No.: ARL-MR-0672.

12. Weinacht P. Coupled CFD/GN&C modeling for a smart material canard actuator. Aberdeen Proving Ground (MD): Army Research Laboratory (US); 2007. Report No.: ARL-TR-4265.

13. Fresconi FE, Celmins I, Silton S, Costello M. High maneuverability projectile flight using low cost components. Aerospace Science and Technology. 2015;41:175–188.

14. Burchett B. Matlab Tools for automated system identification and control design of single-input single-output (SISO) motor loops. Aberdeen Proving Ground (MD): Army Research Laboratory (US); 2017. Report No.: ARL-CR-0817.

15. Sahu J, Fresconi F. Flight behaviors of a complex projectile using a coupled CFD-based simulation technique: free motion. 33rd AIAA Applied Aerodynamics Conference, AIAA Aviation Forum; 2015 June 22–26; Dallas, TX. AIAA Paper No.: 2015-2585.

16. Sahu J, Fresconi F. Flight behaviors of a complex projectile using a coupled CFD-based simulation technique: open-loop control. 54th Aerospace Sciences Meeting, AIAA SciTech Forum. 2016 Jan 4–6; San Diego, CA. AIAA Paper No.: 2016-2025.

17. Gad-el-Hak M, Bushnell DM. Separation Control: Review. Journal of Fluids Engineering. 1991;113:5–30.

## List of Symbols, Abbreviations, and Acronyms

| | |
|---|---|
| 3-D | three-dimensional |
| CAS | control actuation system |
| CFD | computational fluid dynamics |
| CP | center of pressure |
| HMA | high-maneuverability airframe |

| | |
|---|---|
| 1 | DEFENSE TECHNICAL |
| (PDF) | INFORMATION CTR |
| | DTIC OCA |
| | |
| 2 | DIR ARL |
| (PDF) | IMAL HRA |
| | RECORDS MGMT |
| | RDRL DCL |
| | TECH LIB |
| | |
| 1 | GOVT PRINTG OFC |
| (PDF) | A MALHOTRA |
| | |
| 3 | ARL |
| (PDF) | RDRL WML E |
| | J T BRYSON |
| | I CELMINS |
| | F E FRESCONI |